Reynolds stress scaling in the near-wall region of channel, pipe and boundary layer flows

Alexander J. Smits[1], Marcus Hultmark[1], Myoungkyu Lee[2], Sergio Pirozzoli[3] and Xiaohua Wu[4]

[1]Department of Mechanical and Aerospace Engineering, Princeton University, Princeton, NJ 08544, USA

[2]Sandia National Laboratories, Livermore, CA 94551, USA

[3]Dipartimento di Ingegneria Meccanica e Aerospaziale, Università di Roma "La Sapienza," 00184 Roma, Italy

[4]Department of Mechanical and Aerospace Engineering, Royal Military College of Canada, Kingston, Ontario, Canada K7K 7B4

(Received 19 May 2021)

A new scaling is derived that yields a Reynolds number independent profile for all components of the Reynolds stress in the near-wall region of wall bounded flows, including channel, pipe and boundary layer flows. The scaling demonstrates the important role played by the wall shear stress fluctuations and how the large eddies determine the Reynolds number dependence of the near-wall turbulence behavior.

1. Introduction

Here, we examine the near-wall scaling behavior of canonical turbulent flows on smooth surfaces. These flows include two-dimensional zero-pressure gradient boundary layers, and fully developed pipe and channel flows. The focus is on the region $y^+ < 100$, which includes the peaks in the streamwise and spanwise turbulent stresses. Here, y is the distance form the wall, and the superscript $^+$ denotes non-dimensionalization using the fluid kinematic viscosity ν and the friction velocity $u_\tau = \sqrt{\tau_w/\rho}$, where τ_w is the mean wall shear stress and ρ is the fluid density.

For isothermal, incompressible flow, it is commonly assumed that for the region close to the wall

$$[U_i, \overline{u_i u_j}] = f(y, u_\tau, \nu, \delta),$$

where U_i and u_i are the mean and fluctuating velocities in the ith direction. The overbar denotes time averaging, and the outer length scale δ is, as appropriate, the boundary layer thickness, the pipe radius, or the channel half-height. That is,

$$[U_i^+, \overline{(u_i u_j)^+}] = f(y^+, Re_\tau). \tag{1.1}$$

where the friction Reynolds number $Re_\tau = \delta u_\tau/\nu$.

By all indications, the streamwise mean velocity U in the region $y/\delta \lessapprox 0.15$ is a unique function of y^+ that is independent of Reynolds number (see, for example, Zagarola & Smits 1998, and McKeon *et al.* 2004). In contrast, the Reynolds stresses in the near-wall region exhibit a significant dependence on Reynolds number, as illustrated in figure 1

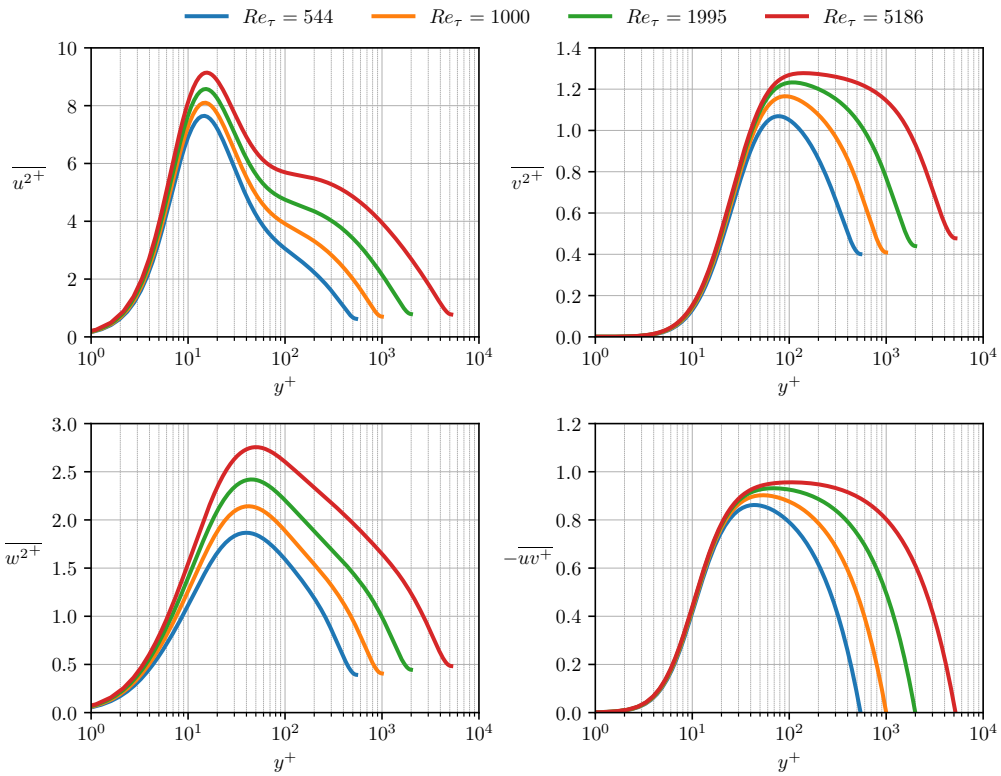

FIGURE 1. Profiles of turbulent stresses in channel flow, as computed by direct numerical simulations (DNS) by Lee & Moser (2015).

for channel flow. Here, $\overline{u^2}$, $\overline{v^2}$ and $\overline{w^2}$ are in the streamwise, wall-normal and spanwise directions, respectively, and $-\overline{uv}$ is the Reynolds shear stress.

The behavior of the streamwise component $\overline{u^{2+}}$ has been a particular focus of attention, especially its peak value $\overline{u_p^{2+}}$ located at $y^+ \approx 15$. By experiment, Samie *et al.* (2018) showed that in a boundary layer over a wide range of Reynolds numbers $\overline{u_p^{2+}}$ follows a logarithmic variation given by

$$\overline{u_p^{2+}} = \beta + \alpha \ln(Re_\tau). \tag{1.2}$$

with $\alpha = 0.646$ and $\beta = 3.54$. Lee & Moser (2015) found a very similar result from DNS of a channel flow (using only the data for $y^+ \geq 1000$) with $\alpha = 0.642$ and $\beta = 3.66$, very much in line with the result reported by Lozano-Durán & Jiménez (2014), also obtained by DNS of channel flow, who found $\alpha = 0.65$ and $\beta = 3.63$. Finally, Pirozzoli *et al.* (2021) found $\alpha = 0.612$ and $\beta = 3.75$ from DNS for pipe flow at Re_τ up to 6000.

We now examine the scaling of the stresses in the near-wall region using DNS for channel flows (Lee & Moser 2015), pipe flows (Pirozzoli *et al.* 2021) and boundary layers (Wu *et al.* 2017). Couette flows were also considered but it turns out that their behavior is very different from the other canonical flows (Pirozzoli *et al.* 2014; Lee & Moser 2017, 2018), and therefore they will be considered separately in a future study.

Need to refer to Monkewitz (2021); Smits & Hultmark (2021); Hultmark & Smits (2021).

	Re_τ	f_{u^2}	$10^3 f_{v^2}$	f_{w^2}	$-10^2 f_{uv}^2$	Ref.
Channel	544	0.164	0.140	0.0679	0.0975	Lee & Moser (2015)
	1000	0.175	0.158	0.0764	0.102	Lee & Moser (2015)
	1995	0.187	0.176	0.0835	0.107	Lee & Moser (2015)
	5186	0.200	0.189	0.0894	0.110	Lee & Moser (2015)
Pipe	495	0.149	0.118	0.0589	0.101	Pirozzoli *et al.* (2021)
	1137	0.168	0.147	0.0718	0.113	Pirozzoli *et al.* (2021)
	1976	0.178	0.158	0.0770	0.120	Pirozzoli *et al.* (2021)
	3028	0.185	0.164	0.0797	0.125	Pirozzoli *et al.* (2021)
	6022	0.195	0.171	0.0837	0.127	Pirozzoli *et al.* (2021)
Boundary layer	500	0.179	0.199	0.0778		Wu *et al.* (2017)
	1000	0.183	0.207	0.0843		Wu *et al.* (2017)

TABLE 1. Flow and Reynolds number dependence of the functions f. Data only for $Re_\tau > 200$.

2. Taylor Series expansions

We begin by writing the Taylor series expansions for u_i in the vicinity of the wall. Instantaneously (Pope 2000; Bewley & Protas 2004),

$$\underline{u}^+ = \underline{a}_1 + \underline{b}_1 y^+ + \underline{c}_1 {y^+}^2 + \underline{d}_1 {y^+}^3 + O({y^+}^4) \tag{2.1}$$

$$\underline{v}^+ = \underline{a}_2 + \underline{b}_2 y^+ + \underline{c}_2 {y^+}^2 + \underline{d}_2 {y^+}^3 + O({y^+}^4) \tag{2.2}$$

$$\underline{w}^+ = \underline{a}_3 + \underline{b}_3 y^+ + \underline{c}_3 {y^+}^2 + \underline{d}_3 {y^+}^3 + O({y^+}^4) \tag{2.3}$$

where $\underline{u} = U + u$, etc. The no-slip condition gives $\underline{a}_1 = \underline{a}_2 = \underline{a}_3 = 0$, and by continuity $\partial v/\partial y|_w = \underline{b}_2 = 0$. Also

$$\underline{b}_1 = (\partial \underline{u}^+/\partial y^+)_w, \tag{2.4}$$

$$\underline{b}_3 = (\partial \underline{w}^+/\partial y^+)_w, \tag{2.5}$$

$$\underline{c}_2 = \tfrac{1}{2}(\partial^2 \underline{v}^+/\partial {y^+}^2)_w = -\tfrac{1}{2}(\partial \underline{b}_1/\partial x^+ + \partial \underline{b}_3/\partial z^+). \tag{2.6}$$

For the corresponding time-averaged quantities

$$\overline{u^{2+}}/{y^+}^2 = f_{u^2} + 2\overline{b_1 c_1}\, y^+ + O({y^+}^2) \tag{2.7}$$

$$\overline{v^{2+}}/{y^+}^4 = f_{v^2} + 2\overline{c_2 d_2}\, y^+ + O({y^+}^2) \tag{2.8}$$

$$\overline{w^{2+}}/{y^+}^2 = f_{w^2} + 2\overline{b_3 c_3}\, y^+ + O({y^+}^2) \tag{2.9}$$

$$\overline{uv^+}/{y^+}^3 = f_{uv} + (\overline{b_1 d_2} + \overline{c_1 c_2})\, y^+ + O({y^+}^2) \tag{2.10}$$

where we use the notation $f_{u^2} = \overline{b_1^2}$, $f_{v^2} = \overline{c_2^2}$, $f_{w^2} = \overline{b_3^2}$, and $f_{uv} = \overline{b_1 c_2}$.

These functions all become constant as the wall is approached, and the values of f_{u^2}, f_{v^2}, f_{w^2} and f_{uv} are given by their intercepts at $y^+ = 0$, as illustrated in figure 2 for channel flow. Similar results are obtained for the other two flows, and the values are listed in table 1. For the boundary layer flow the values were acquired by fitting the DNS data in the region $y^+ < 3$ with a fourth-order polynomial.

The Reynolds number dependence of the functions f is shown in figure 3. They all increase with Reynolds number, but at a given Reynolds number their values increase as we move from pipe to channel to boundary layer, except for f_{uv} where the pipe flow values are larger than the channel flow values. These trends will be discussed further in § 4.

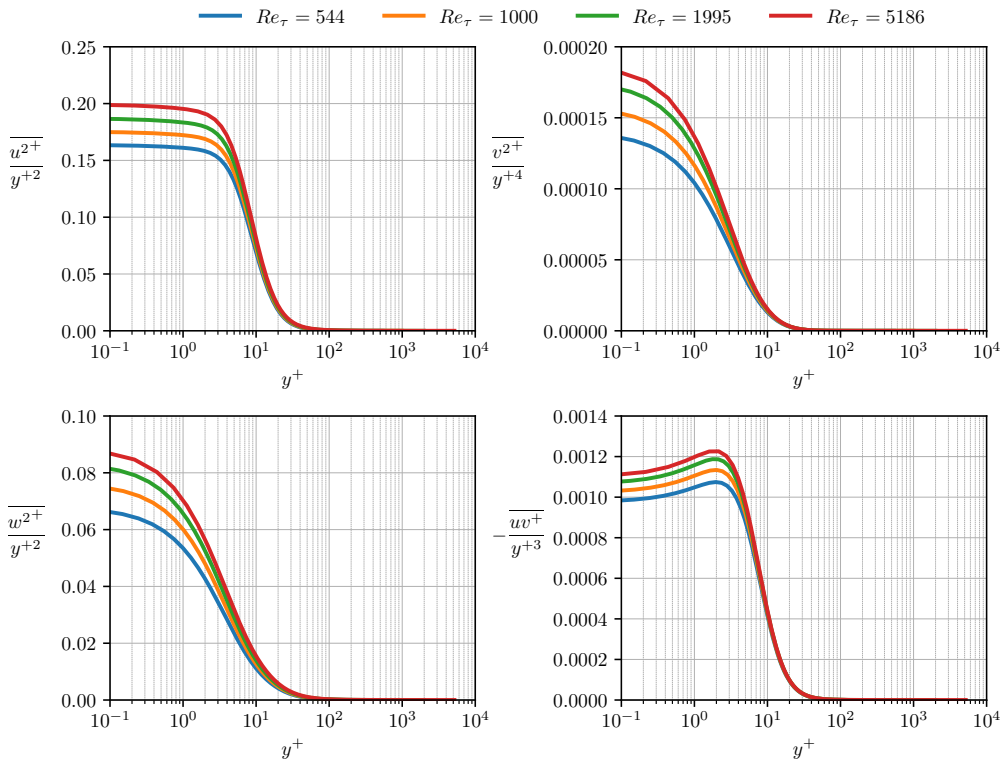

FIGURE 2. Top left: Profiles of $\overline{u^{+2}}/y^{+2}$; intercept at $y^+ = 0$ is f_{u^2}. Top right: Profiles of $\overline{v^{+2}}/y^{+4}$; intercept at $y^+ = 0$ is f_{v^2}. Bottom left: Profiles of $\overline{w^{+2}}/y^{+2}$; intercept at $y^+ = 0$ is f_{w^2}. Bottom right: Profiles of $(-\overline{uv^+})/y^{+3}$; intercept at $y^+ = 0$ is $-f_{uv}$. From DNS of channel flow (Lee & Moser 2015).

3. Scaling the streamwise stress profiles

If we now scale each $\overline{u^{+2}}$ profile with the value of f_{u^2} at the same Reynolds number, we obtain the results shown in figure 4. For all three flows, the collapse of the data for $y^+ < 20$ is impressive, including the almost exact agreement on the scaled inner peak value. In fact, from table 2 it is evident that with increasing Reynolds number f_{u^2} and $\overline{u_p^{+2}}$ for the channel and pipe flows approach a constant ratio to each other such that

$$\overline{u_p^{+2}} \approx 46 f_{u^2}. \tag{3.1}$$

A similar conclusion was made previously by Agostini & Leschziner (2018) and Chen & Sreenivasan (2021). In other words, the magnitude of the peak at $y^+ \approx 15$ tracks almost precisely with f_{u^2}, a quantity that is evaluated at $y^+ = 0$.

What about the scaling of $\overline{u_p^{+2}}$ in boundary layers? Although the collapse of the data shown in figure 4 is encouraging, the DNS data only cover a small Reynolds number range, too small to make any definite conclusions about the scaling. We can use high Reynolds number experimental data instead, but we need to know what values of f_{u^2} should be used. The highest Reynolds number experiments that are fully resolved are those by Samie *et al.* (2018), but even then data are not available for $y^+ < 5$, so the values of f_{u^2} cannot be obtained directly from the data. In this respect, we note that for

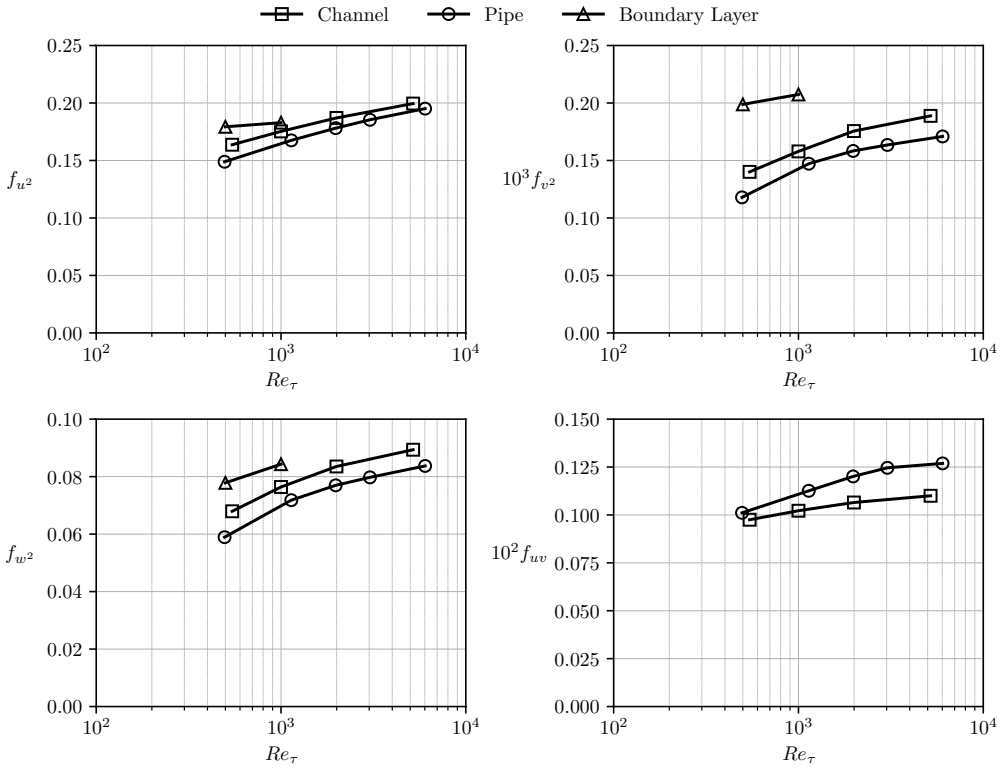

FIGURE 3. Reynolds number variations of functions f. Top left: f_{u^2}. Top right: $10^3 f_{v^2}$. Bottom left: f_{w^2}. Bottom right: $10^2 f_{uv}$. □, channel; ○, pipe; △, boundary layer. Lines for visual aid only. Values given in table 1.

channel flow the variation of f_{u^2} for $Re_\tau > 1000$ is close to logarithmic, so that

$$f_{u^2} = \beta_f + \alpha_f \ln Re_\tau \tag{3.2}$$

where $\beta_f = 0.08$ and $\alpha_f = 0.0139$. For pipe flow, a similar relationship with a slightly smaller offset (0.074) appears to fit the data for $Re_\tau > 3000$, but the Reynolds number range is too small to make any definite conclusions. If we simply assume that the channel flow relationship given by equation 3.2 can be used to find the right values of f_{u^2} for high Reynolds number boundary layers, then we obtain the results shown in figure 5. We see a clear collapse of the data for $y^+ < 20$, and so it appears that the near-wall profiles of $\overline{u^{2+}}$ for boundary layers, pipes and channel flows all collapse in this scaling.

What about the inverse? Figure 6 shows the variation of the peak streamwise turbulence intensity $\overline{u_p^{2+}}$ with Re_τ for boundary layers at lower Reynolds numbers. It is seen that the correlation developed by (Samie *et al.* 2018) based on experimental data from $6000 < Re_\tau < 20000$ agrees very well for the DNS data over a much lower Reynolds number range (at least for $Re_\tau > 400$). It is thus reasonable to expect the channel flow DNS correlation developed by Lee & Moser (2015) for $544 < Re_\tau < 5186$ can be used to predict the behavior of $\overline{u_p^{2+}}$ in turbulent channel flows at much higher Reynolds numbers.

We can now make some observations on mixed flow scaling. DeGraaff & Eaton (2000) proposed that the correct scaling for $\overline{u^2}$ in boundary layers should be $\overline{u^{2+}}\sqrt{C_f/2}$, where the skin friction coefficient $C_f = \frac{1}{2}\tau_w/\rho U_e^2$ and U_e is the mean velocity at the edge of

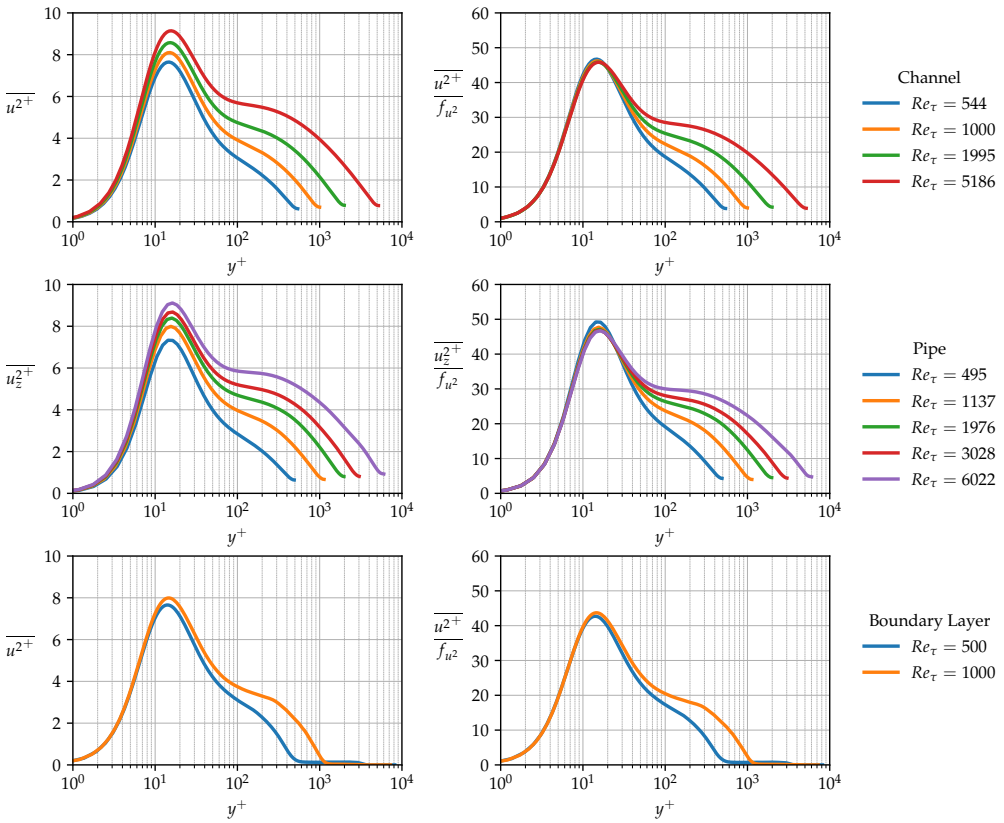

FIGURE 4. Profiles of streamwise stresses. Left column: conventional scaling. Right column: f-scaling. Top row: channel flow (Lee & Moser 2015). Second row: pipe flow (Pirozzoli *et al.* 2021). Third row: boundary layer flow (Wu *et al.* 2017).

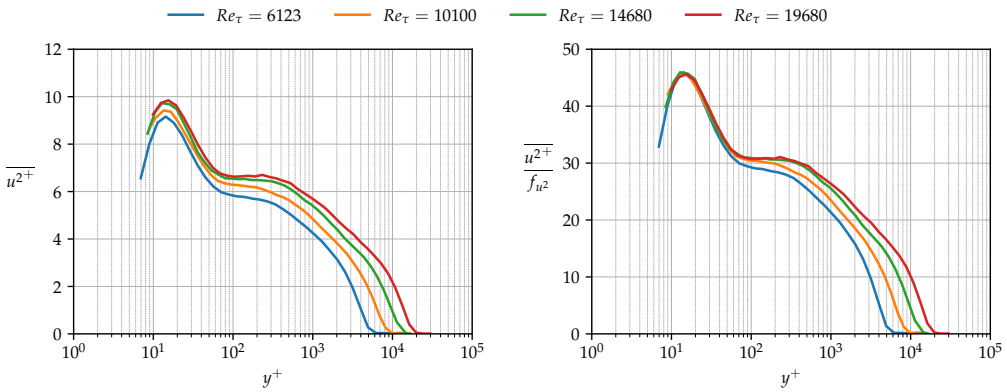

FIGURE 5. Scaled boundary layer experiments. Left: From Vallikivi *et al.* (2015) for Re_τ = 2,622 to 72,526. Right: From Samie *et al.* (2018) for Re_τ = 6,123 to 19,680.

	Re_τ	$\overline{u_p^{+2}}$	y_{up}^+	$\frac{\overline{u_p^{+2}}}{f_{u^2}}$	$\frac{f_{u^2}u_\tau}{U_b}$	$\overline{w_p^{+2}}$	$\frac{\overline{w_p^{+2}}}{f_{w^2}}$	$-\overline{uv_p^+}$	$(-\overline{uv_p^+})_s$	$\overline{v_p^{+2}}$
Channel	544	7.65	14.8	46.7	0.00890	1.87	27.5	0.862	1.00	1.07
	1000	8.10	15.2	46.2	0.00877	2.14	28.0	0.903	1.01	1.17
	2003	8.58	15.3	45.9	0.00858	2.42	29.0	0.932	1.00	1.23
	5186	9.14	15.7	45.8	0.00828	2.76	30.8	0.956	1.00	1.28
Pipe	495	7.35	14.3	49.4	0.00867	1.78	30.3	0.852	1.00	1.05
	1137	8.00	15.5	47.7	0.00865	2.15	20.0	0.907	1.00	1.18
	1976	8.40	16.0	47.2	0.00854	2.37	30.7	0.931	1.00	1.23
	3028	8.68	16.4	46.8	0.00844	2.52	31.7	0.943	1.00	1.26
	6022	9.12	16.2	46.7	0.00824	2.77	33.0	0.959	1.00	1.29
Boundary layer (DNS)	500	7.66	13.9	42.7	0.00817	1.86	23.9	0.917	1.07	1.12
	1000	7.99	14.8	43.7	0.00737	2.11	25.0	0.935	1.04	1.25
Boundary layer (Experiment)	6123	9.16	14.3							
	10100	9.44	14.5							
	14680	9.75	13.6							
	19680	9.85	14.8							

TABLE 2. Scaling the inner peak maximum values $\overline{u_p^{+2}}$, $\overline{w_p^{+2}}$, $-\overline{uv_p^+}$ and $\overline{v_p^{+2}}$. Here, $(-\overline{uv_p^+})_s = -\overline{uv_p^+}/(1-2/\sqrt{\kappa Re_\tau})$ with $\kappa = 0.384$. Channel flow data from Lee & Moser (2015); pipe flow data from Pirozzoli *et al.* (2021); boundary layer data from Wu *et al.* (2017) and Samie *et al.* (2018). Xiaohua, I thought uv data is not available because I didn't see it in the previous table. Is it available?

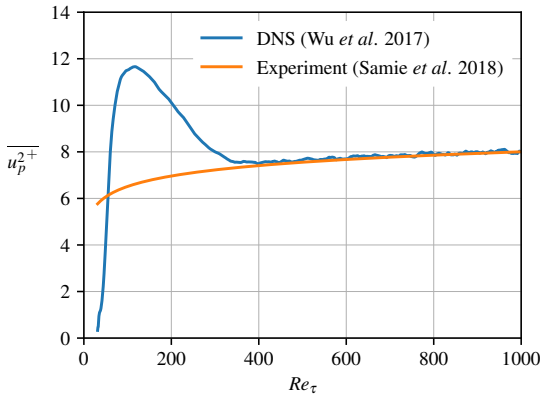

FIGURE 6. Variation of $\overline{u_p^{2+}}$ with Reynolds number in boundary layers. Blue line: DNS (Wu *et al.* 2017); orange line: experiment (Samie *et al.* 2018). Shouldn't this be marked as equation 1.2 with $\alpha = 0.646$ and $\beta = 3.54$.? The one that fits Samie's experimental data and everybody else?

the layer. This is equivalent to scaling $\overline{u^2}$ with $u_\tau U_e$ (hence the term mixed scaling). If this is correct, then $f_{u^2}u_\tau/U_e$ needs to be invariant with Reynolds number. As seen from table 2 this is not so, and despite the apparent collapse of their data for $540 < Re_\tau < 10{,}000$ using $u_\tau U_e$, mixed scaling is only an approximation to the correct scaling for the inner region. Note differences between f and C_f in going from internal flows to external flows, and whether it affects the mixed scaling analysis. That is, U_e versus U_{CL} or U_b.

We should also note that the position of the peak in the streamwise stress, denoted by y_{up}^+, is listed in table 2. For all flows, including the high Reynolds number experiments,

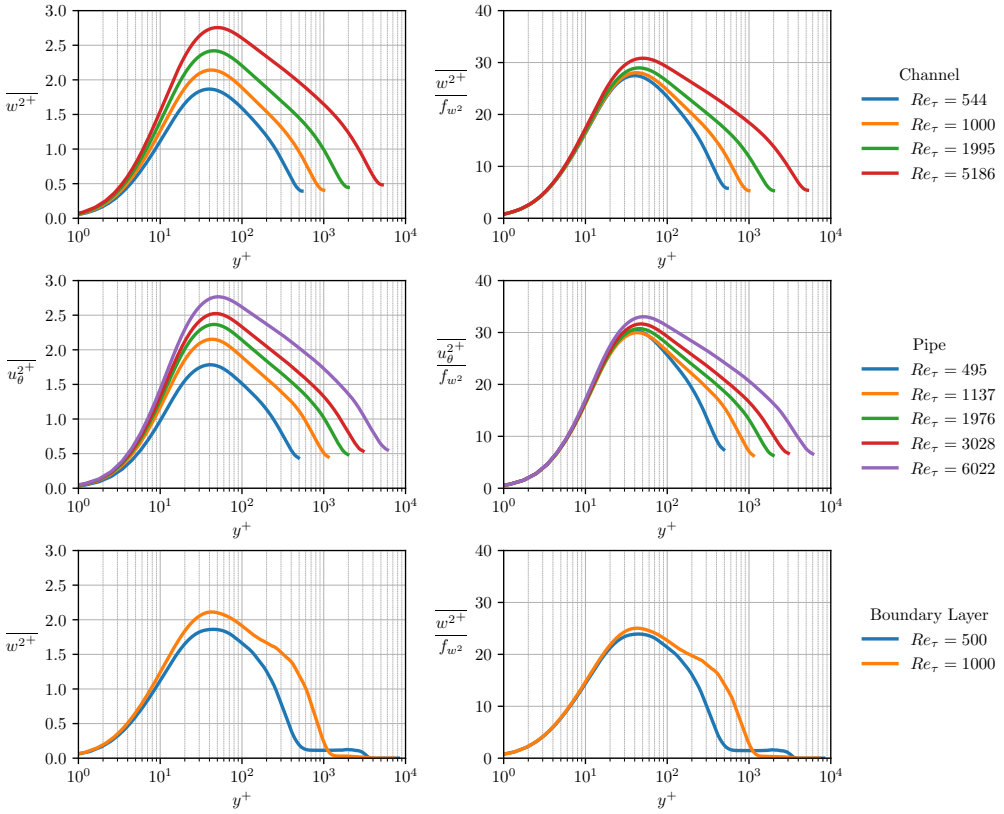

FIGURE 7. Profiles of spanwise stresses. Left column: conventional scaling. Right column: f-scaling. Top row: channel flow (Lee & Moser 2015). Second row: pipe flow (Pirozzoli *et al.* 2021). Third row: boundary layer flow (Wu *et al.* 2017).

the value is constant at 15 $\pm$1.5 (the uncertainty is similar to that set by the resolution of the data in this region). This value is in accord with most previous estimates.

4. Scaling the other stress profiles

When the $\overline{w^{+2}}$ profiles are scaled with the value of f_{w^2} at the same Reynolds number, we obtain the results shown in figure 7. The data collapse well for $y^+ < 20$, but the scaling does not capture the peak value. From table 2 we see that the ratio between $\overline{w_p^{+2}}$ and f_{w^2} is a slowly increasing function of Reynolds number, and no asymptotic behavior is apparent, at least over this Reynolds number range. In addition, the location of the peak moves away from the wall with increasing Reynolds number for all three flows. Thus, for the streamwise and spanwise stresses, the scaling is appropriate only for $y^+ < 20$ (hence it can capture the peak for $\overline{u^{+2}}$ but not for $\overline{w^{+2}}$).

As for the $\overline{v^{+2}}$ profiles shown in figure 8, scaling by f_{v^2} brings no particular improvement over the unscaled data, even for $y^+ < 20$. An explanation for this behavior is advanced in § 4. However, it is clear that the unscaled data develops a plateau with increasing Reynolds number. The height of this plateau may be characterized by the peak value of $\overline{v^{+2}}$, and these values are given in table 2 as $\overline{v_p^{+2}}$. For the channel and pipe flows,

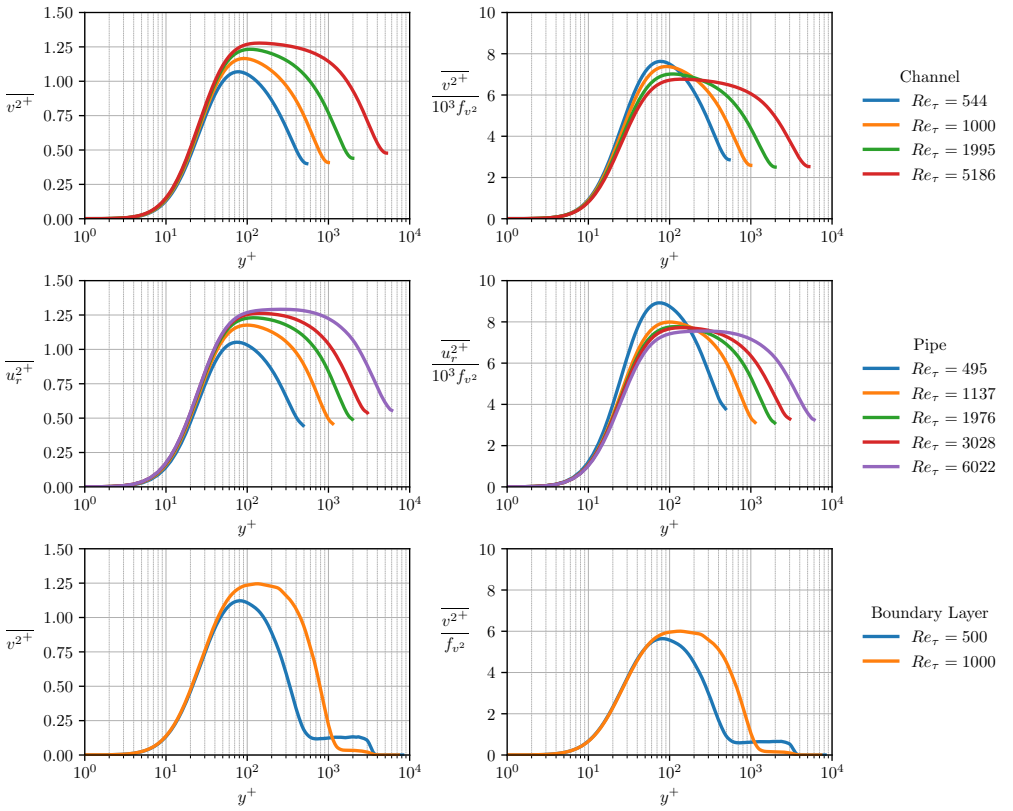

FIGURE 8. Profiles of wall-normal stresses. Left column: conventional scaling. Right column: f-scaling. Top row: channel flow (Lee & Moser 2015). Second row: pipe flow (Pirozzoli *et al.* 2021). Third row: boundary layer flow (Wu *et al.* 2017).

the level of the plateau appear to approach about 1.3 with increasing Reynolds number. The experiments by DeGraaff & Eaton (2000) at Reynolds numbers up to 10,070 suggest a slightly higher level, closer to about 1.4. This number corresponds to the constant A_2 in Townsend's scaling of the wall-normal fluctuations in the logarithmic region, as derived from the attached eddy hypothesis (Townsend 1976).

The shear stress profiles shown in figure 8 display a somewhat similar behavior to the normal stress distributions, in that the proposed scaling does not offer much improvement over the unscaled data, and that a broad plateau appears with increasing Reynolds number. However, for the pipe and channel flows the extent of the plateau must be bounded at its outer limit by the linear decrease in shear stress dictated by the streamwise pressure gradient. Its maximum value also cannot exceed one. However, it is rather satisfying to see that the scaling for the peak value proposed by Lee & Moser (2015) for channel flow, that is, $(-\overline{uv_p^+})_s = -\overline{uv_p^+}/(1 - 2/\sqrt{\kappa Re_\tau})$ with $\kappa = 0.384$ works very well for both channel and pipe flow, as shown in table 2.

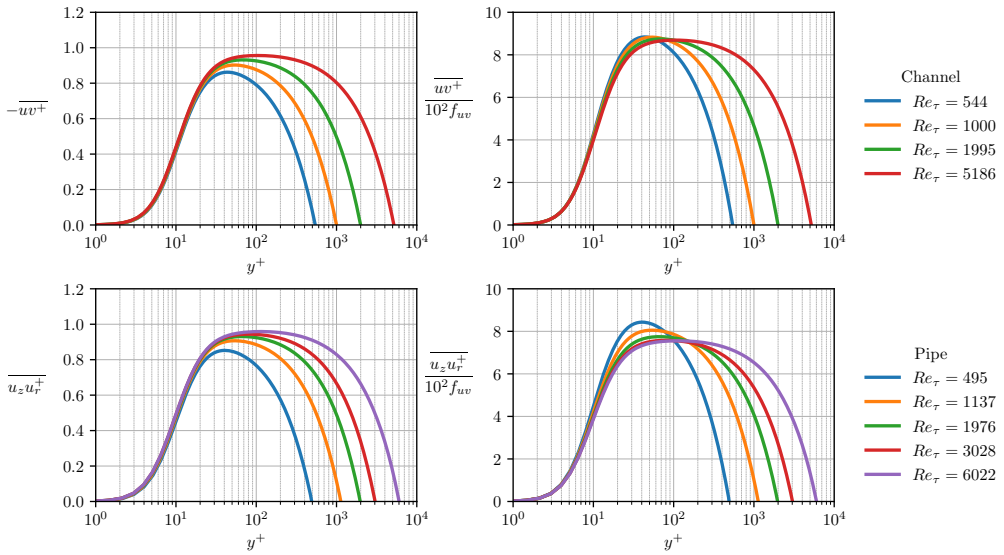

FIGURE 9. Profiles of shear stresses. Left column: conventional scaling. Right column: f-scaling. Top row: channel flow (Lee & Moser 2015). Second row: pipe flow (Pirozzoli *et al.* 2021).

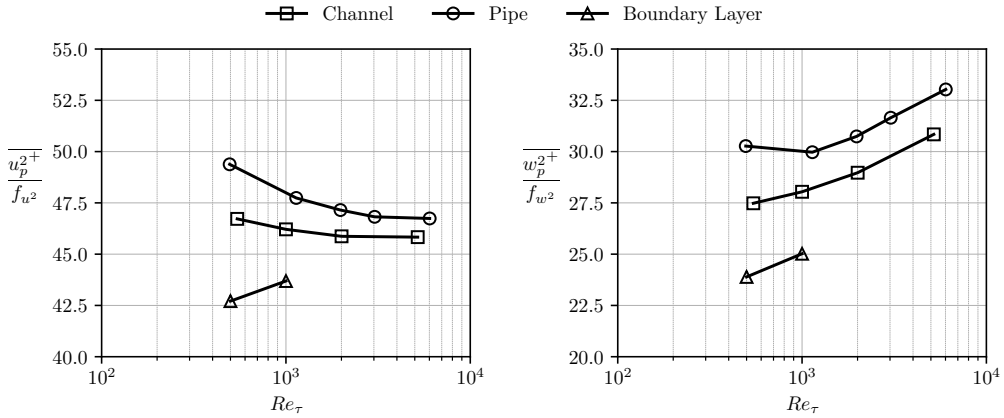

FIGURE 10. Scaled stresses. Left: $\overline{u_p^{+2}}/f_{u^2}$. Right: $\overline{w_p^{+2}}/f_{w^2}$. □, channel; ○, pipe; △, boundary layer. Lines for visual aid only. Values given in table 2.

5. What does it all mean?

The Taylor series expansion revealed that

$$f_{u^2} = \overline{b_1^2} = \overline{\left(\frac{\partial u^+}{\partial y^+}\right)_w^2} = \frac{\overline{\tau'^2_{wx}}}{\tau_w^2} \tag{5.1}$$

$$f_{w^2} = \overline{b_3^2} = \overline{\left(\frac{\partial w^+}{\partial y^+}\right)_w^2} = \frac{\overline{\tau'^2_{wz}}}{\tau_w^2}. \tag{5.2}$$

For wall-bounded flows, therefore, the controlling parameter in the near-wall scaling for u is the mean square of the fluctuating wall stress in the x-direction τ'_{wx}, and for w it is the mean square of the fluctuating wall stress in the z-direction τ'_{wz}.

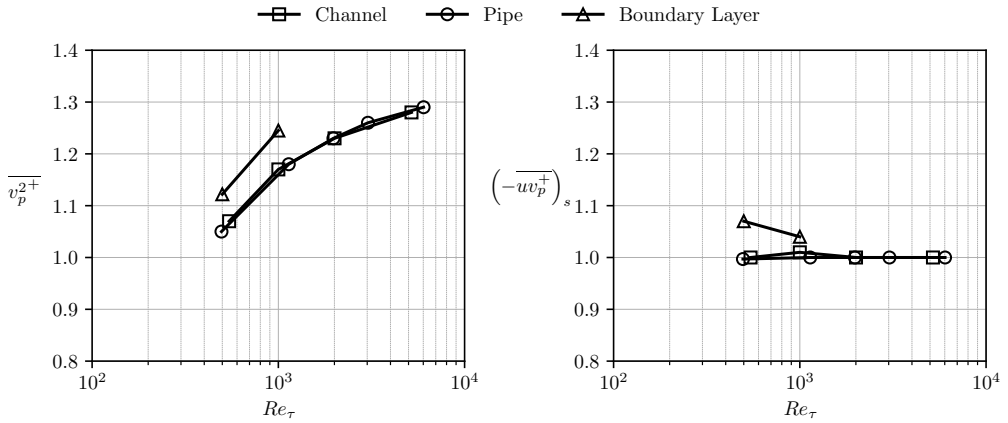

FIGURE 11. Scaled shear stress $(-\overline{uv_p^+})_s$ (Left) and peak wall normal stress $\overline{v_p^{+2}}$ (right). □, channel; ○, pipe; △, boundary layer. Values given in table 2.

For the other two functions, the Taylor series expansion gives

$$f_{v^2} = \overline{c_2^2} = \tfrac{1}{4}\overline{\left(\frac{\partial^2 \underline{v}^+}{\partial y^{+2}}\right)_w^2} = -\tfrac{1}{2}\overline{\left(\frac{\partial b_1}{\partial x^+} + \frac{\partial b_3}{\partial z^+}\right)^2} \tag{5.3}$$

$$f_{uv} = \overline{b_1 c_2} \tag{5.4}$$

where b_1, b_3 and c_2 are the fluctuating parts of $\underline{b}_1$, $\underline{b}_3$ and $\underline{c}_2$, as given in equations 2.4-2.6. The functions f_{v^2} and f_{uv} therefore express correlations between spatial gradients of the instantaneous wall stress fluctuations, as well as the fluctuating wall stress itself, and so it is more difficult to give a precise meaning to f_{v^2} and f_{uv}, but they are clearly more connected to the small-scale motions than either f_{u^2} or f_{w^2}. However, by continuity, we see that it is essentially the gradients of the fluctuating shear stress (b_1 and b_2) that give rise to the wall-normal motion through continuity.

This connection with the fluctuating wall stress helps to explain the Reynolds number dependence of the functions f shown in figure 3 because with increasing Reynolds number the large-scale (outer layer) motions contribute more and more to the fluctuating wall stress by modulation and superimposition of the near-wall motions (Marusic *et al.* 2010; Agostini & Leschziner 2018), as may be seen from the pre-multiplied wall stress spectra shown in figure 12. Of course, it is the turbulence that controls the wall stress, and not vice versa, but the main point is that the whole of the region $y^+ < 20$ (including the peak in $\overline{u^{2+}}$) scales with the velocity scale $u_s = u_\tau\sqrt{f_{u^2}}$, which can be determined by measuring the fluctuating wall stress, a clear indication of the increasingly important contribution of the large-scale motions on the near wall behavior as the Reynolds number increases. Because f_{v^2} and f_{uv} are more connected to the small-scale motions than either f_{u^2} and f_w^2, it might be expected that they feel the effects of modulation more than superimposition by the large-scale motions (Marusic *et al.* 2010).

An interpretation based on dissipation scaling rather than wall stress scaling was offered by Chen & Sreenivasan (2021). By using the energy budget for $\overline{u^{2+}}$, they noted that $\sqrt{f_u^2}$ equals the dissipation rate at the wall, $\epsilon_{u_w}^+$. What's more, close to the wall, the dissipation is balanced by viscous transport, and all other terms are small, as illustrated for channel flow in figure 13. According to Chen & Sreenivasan (2021), this leads to two

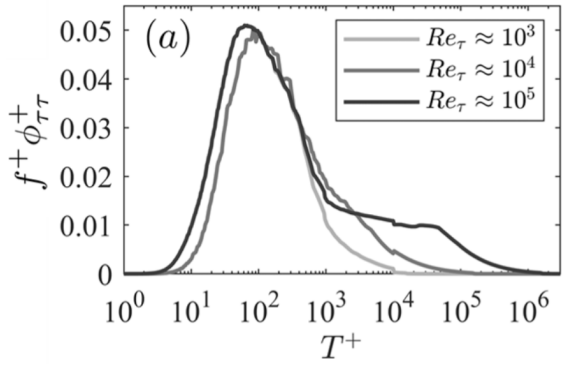

FIGURE 12. Pre-multiplied spectra of the wall stress fluctuations τ'_w at $Re_\tau \approx 10^3$, 10^4, and 10^5 ($T^+ = 1/f^+ = u_\tau^2/(f\nu)$, f is the frequency in Hz). Data taken from DNS of del Álamo *et al.* (2004), hot-wire measurements, and predictive models (Marusic *et al.* 2010; Mathis *et al.* 2013; Chandran *et al.* 2020). From Marusic *et al.* (2020).

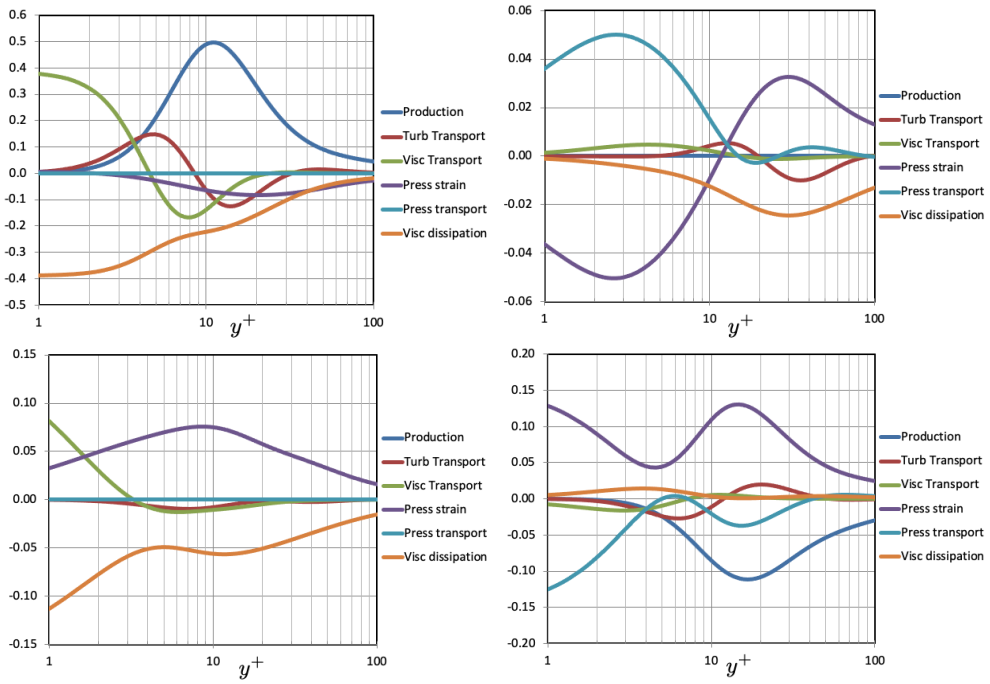

FIGURE 13. Energy budgets for turbulent stresses in channel flow at $Re_\tau = 5186$ (Lee & Moser 2015). Top left: $\overline{u^{2+}}$. Top right: $\overline{v^{2+}}$. Bottom left: $\overline{w^{2+}}$. Bottom right: $-\overline{uv}^+$.

conclusions. The first is that the order of the peak value of $\overline{u^{2+}}$ can be estimated as $\epsilon^+_{u_w} y_p^+$, which yields the same result given in equation 3.1. The second is that the dissipation must be bounded at infinite Reynolds number, and so the logarithmic increase in $\sqrt{f_u^2}$ (equation 3.2), and by extension the logarithmic increase in $\overline{u_p^{2+}}$ (equation 1.2), need to be reconsidered. They then suggest an alternative formulation for the peak magnitude that approaches a finite limit at infinite Reynolds number, based on the Reynolds number dependence of the dissipation.

However, figure 13 shows that the energy balance for $\overline{u^{2+}}$ changes rapidly with distance

from the wall, so that by $y^+ = 10$ the production dominates, and that the viscous transport has actually changed sign. It is not clear, therefore, why a dissipation scaling should persist all the way to $y^+ = 20$, as demonstrated here. Our interpretation, based on the wall stress signature, has the benefit of reflecting more accurately the influence of the large-scale motions in the near-wall region, and so may offer a more robust explanation for the near-wall scaling. Note that the dissipation of u^2 also shows Re dependencies (Figure **??**) and it is mainly from the contribution of large-scale motions increases with Re. Interestingly, this behavior diminishes at $y^+ \approx 20$ (Lee & Moser 2019). As Re increases, the energy in large-scale motions produced in the log-layer transported to the buffer layer by turbulent transport and the energy in large-scale motions are transported to the viscous sublayer by viscous transport mechanism. Finally, the energy in large-scale motions get dissipated by high $(\partial u/\partial y)^2$. Note also that the produced energy in relatively small scale motions, which has peak at $y^+ \approx 15$, is transfered to the large-scale motion by inverse energy transfer mechanism in the near-wall region (Lee & Moser 2019).

The energy budget for $\overline{w^{2+}}$ also shows that very close to the wall that the viscous transport is balanced by dissipation $\epsilon^+_{w_w}$. However, by about $y^+ \approx 3$, the balance changes so that now pressure strain balances the dissipation and all other terms are small. It seems more natural therefore to build a scaling argument on the behavior of the wall stress fluctuations rather than the dissipation.

The energy budgets for $\overline{v^{2+}}$ and $-\overline{uv^+}$ (also shown in figure 13) show that for both stresses very close to the wall the pressure strain is balanced by pressure transport, which must go to zero at the wall which is explained as 'splat' effect. For $\overline{v^{2+}}$, the balance changes rapidly with distance from the wall so that by $y^+ > 10$ the pressure strain/dissipation balance dominates. Even more interestingly, for $-\overline{uv^+}$ dissipation is not important anywhere in the near-wall region and for $y^+ > 10$ the pressure strain/production balance dominates.

6. Two-dimensional spectral density of f_{u^2}, f_{v^2}, f_{w^2}, f_{uv}

To understand more deeply the influence of the large scale motions on the fluctuations in the wall stress, we examine the spectral structure of the proposed scaling parameters. The spectral densities of the functions f's are given by

$$E_{f_{u^2}}(k_x, k_z) = 2\mathrm{Re}\{\overline{\widehat{b_1}\widehat{b_1}^*}\} \tag{6.1}$$

$$E_{f_{v^2}}(k_x, k_z) = 2\mathrm{Re}\{\overline{\widehat{c_2}\widehat{c_2}^*}\} \tag{6.2}$$

$$E_{f_{w^2}}(k_x, k_z) = 2\mathrm{Re}\{\overline{\widehat{b_3}\widehat{b_3}^*}\} \tag{6.3}$$

$$E_{f_{uv}}(k_x, k_z) = 2\mathrm{Re}\{\overline{\widehat{b_1}\widehat{c_2}^*}\} \tag{6.4}$$

where $\hat{\cdot}$ denotes Fourier transformation in the x and z directions, and $\hat{\cdot}^*$ denotes the complex conjugate of $\hat{\cdot}$. Also, k_x and k_z are the wavenumbers in the x and z directions, respectively. We will use the polar-log coordinate system introduced by Lee & Moser (2019) to investigate the spectral structure in terms of length scales and anisotropy. In this approach, the two-dimensional spectral densities in Cartesian coordinates (k_x, k_z) are mapped to the polar-log coordinates $(k_x^\sharp, k_z^\sharp)$ with corresponding Jacobians. For example,

$$f_{u^2} = \iint E_{f_{u^2}} \mathrm{d}k_x \mathrm{d}k_z = \iint \frac{|k|^2}{\xi} E_{f_{u^2}} \mathrm{d}k_x^\# \mathrm{d}k_z^\#, \tag{6.5}$$

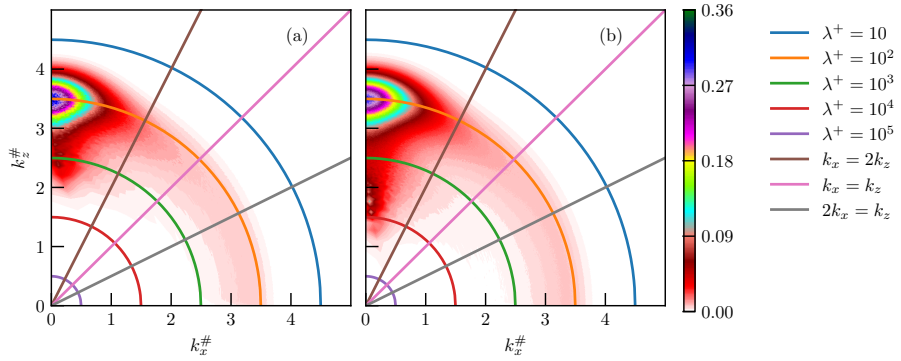

FIGURE 14. Two-dimensional spectral density of f_{u^2} in channel flow, using the DNS by Lee & Moser (2015). Left: $Re_\tau = 1000$. Right: $Re_\tau = 5186$

and

$$k_x^\# = \frac{k_x}{|k|}\xi, \quad k_z^\# = \frac{k_z}{|k|}\xi, \tag{6.6}$$

where

$$|k| = \sqrt{k_z^2 + k_z^2} \quad \text{and} \quad \xi = \log_{10}\frac{|k|}{k_{\text{ref}}}. \tag{6.7}$$

In this form, the anisotropy of the spectral density and the contributions of $k_x = 0$ and $k_z = 0$ are clearly represented. The more commonly used premultiplied two-dimensional spectral density, $k_x k_z E(\log k_x, \log k_z)$ suppresses the contribution to the spectral density when either k_x or k_z is small, thereby masking the influence of the large scale motions. We will choose the reference wavenumber $k_{\text{ref}} = 50000/Re_\tau$. More details on the representation of two-dimensional spectral densities in the polar-log coordinate system are given by Lee & Moser (2019).

The spectral densities of f_{u^2}, shown in figure 14, clearly indicate that streamwise elongated motions ($2k_x < k_z$) dominate the energy content. Also, motions with $\lambda^+ \approx 100$ make the largest contributions, which is consistent with the spectral density of u'^2 has a peak at $\lambda_z^+ = 100$ in the near-wall flows, corresponding to the spacing of the near-wall streaks. Furthermore, with increasing Reynolds number the contributions by the large-scale motions increase; compare, for example, the contributions by motions with $\lambda^+ > 1000$, a trend that is consistent with previous work (Cimarelli *et al.* 2015; Lee & Moser 2019).

to quantify the contributions of large-scale motions and small-scale motions to $E_{f_{u^2}}$, we use a high-pass filter according to

$$f_{u,SS}^2 = \int_{|\mathbf{k}|>k_c} E_{f_{u^2}} \mathrm{d}\mathbf{k}, \tag{6.8}$$

where k_c is the cut-off frequency. For the high Reynolds number case shown in figure 14b, a convenient demarcation between small-scale and large-scale motions occurs at $\lambda^+ \approx 1000$, and so we choose $k_c^+ = 2\pi/1000$. The results are given in figure 15. Whereas f_{u^2} increases with Reynolds number, as shown earlier in figure 3, the small-scale contribution $f_{u,SS}^2$ is almost invariant. Because the small-scale motions ($\lambda^+ < 1000$) are universal in the near-wall region (Lee & Moser 2019), we conclude that f_{u^2} is the correct scaling parameter for near-wall flows at high Reynolds number since it correctly measures the contributions by large-scale motions.

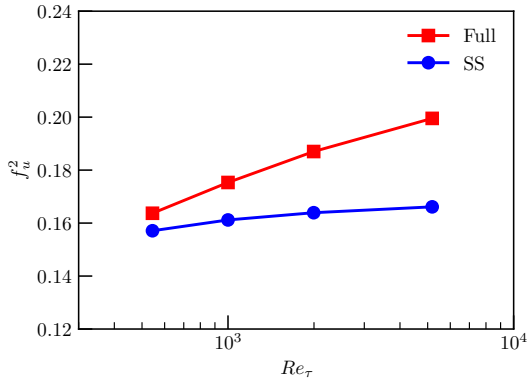

FIGURE 15. Contribution of small-scale motions to f_u^2 in channel flow, using the DNS by Lee & Moser (2015).

The spectral densities of f_{v^2}, f_{w^2} and f_{uv} are shown in figure 16. Only f_{w^2} shows an increasing contribution of large-scale motions as the Reynolds number increases, but it is weak relative to what was seen for f_{u^2}. Both f_{v^2} and f_{w^2} has growing peak intensities with Re at the fixed length scales. The peaks of $E_{f_{w^2}}$ are in smaller length scale than $\lambda^+ = 100$, which is the peak location of $E_{f_{u^2}}$, and the peaks of $E_{f_{v^2}}$ are in much smaller length scales. Also, although $E_{f_{v^2}}$ and $E_{f_{w^2}}$ shows strong streamwise-elongated structure, the relative contributions of spanwise elongated motions are greater in $E_{f_{w^2}}$ and greatest in $E_{f_{v^2}}$.

As to the spectral densities of f_{uv}, there is a negative contribution where $2k_x > k_z$. Similar features are seen in the spectral densities of $u'v'$ (Lee & Moser 2019), but the underlying mechanism of this negative contribution is not clear.

7. Conclusions

By expanding the velocity in a Taylor Series with distance from the wall, the Reynolds number dependence of the near-wall distributions of the Reynolds stresses was traced to the magnitude of the fluctuating wall shear stress and its spatial gradients, which are increasingly affected by the superimposition and modulation of the near-wall motions due to large-scale, outer-layer motions as the Reynolds number increases (Marusic *et al.* 2010).

The Taylor series expansion also suggests a separate scaling for each component of the Reynolds stress. For the streamwise and spanwise components, the scaling collapses the data for $y^+ < 20$, a region that includes the near-wall peak in $\overline{u^{2+}}$ but not the one in $\overline{w^{2}}^{2}$. For the wall-normal component and the Reynolds shear stress, the proposed scaling does not especially improve the collapse of the data, but neither does it degrade the collapse.

Revisiting the dimensional analysis given in equation 1.1, we can now be more precise and write for the Reynolds stresses in a two-dimensional wall-bounded flow, for the region $y^+ < 20$,

$$\overline{(u_i u_j)^+} = f(Re_\tau) g(y^+), \tag{7.1}$$

That is, it is possible to separate the dependence on Reynolds number from the dependence on wall distance.

It may also be remarked that because the scaling is different for each component of the

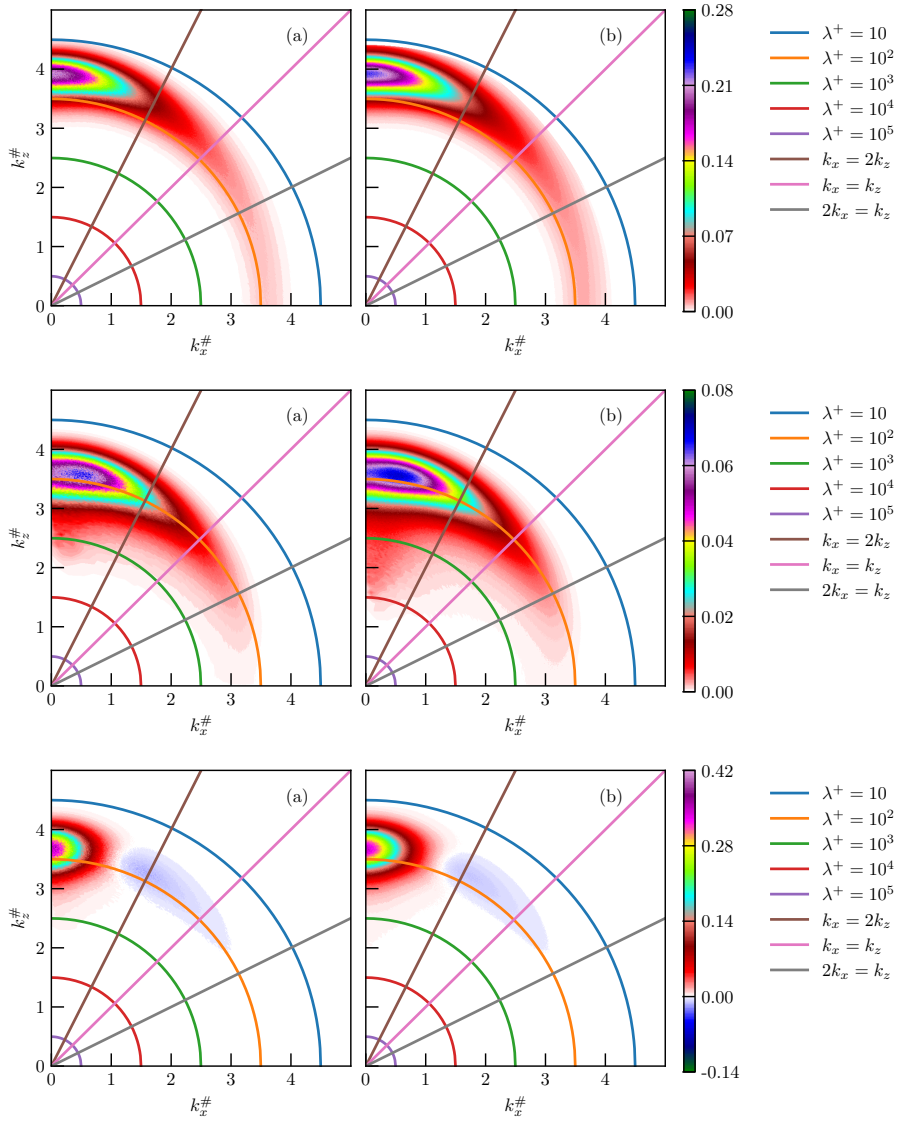

FIGURE 16. 2D spectral density of fs in channel flow (Lee & Moser 2015). Left: $Re_\tau = 1000$. Right: $Re_\tau = 5186$. Top row: $10^3 f_{v^2}$. Middle row: f_{w^2}. Bottom row: $-10^2 f_{uv}$.

stress, any isotropic definition of eddy viscosity will obviously fail in the near-wall region. In this respect, Hultmark *et al.* (2013) noted that in the overlap region, where both the mean velocity U and the streamwise stress $\overline{u^{2+}}$ follow a logarithmic distribution, $\overline{u^{2+}}$ depends on U rather than its gradient.

The authors perceive no conflict of interest in submitting this manuscript.

Acknowledgments

This work was supported by ONR under Grant N00014-17-1-2309 (Program Manager Peter Chang). This research used resources of the Argonne Leadership Computing Facility, which is a DOE Office of Science User Facility supported under Contract DE-AC02-06CH11357. This paper describes objective technical results and analysis. Any subjective

views or opinions that might be expressed in the paper do not necessarily represent the views of the U.S. Department of Energy or the United States Government.

We would like to thank Matt Fu and Liuyang Ding for comments on an earlier draft. Please add acknowledgements as desired.

REFERENCES

Agostini, L. & Leschziner, M. 2018 The impact of footprints of large-scale outer structures on the near-wall layer in the presence of drag-reducing spanwise wall motion. *Flow, Turbulence and Combustion* **100** (4), 1037–1061.

del Álamo, J. C., Jiménez, J., Zandonade, P. & Moser, R. D. 2004 Scaling of the energy spectra of turbulent channels. *J. Fluid Mech.* **500**, 135–144.

Bewley, T. R. & Protas, B. 2004 Skin friction and pressure: the "footprints" of turbulence. *Physica D: Nonlinear Phenomena* **196** (1-2), 28–44.

Chandran, D., Monty, J. P. & Marusic, I. 2020 Spectral-scaling-based extension to the attached eddy model of wall turbulence. *Phys. Rev. Fluids* **5** (10), 104606.

Chen, X. & Sreenivasan, K. R. 2021 Reynolds number scaling of the peak turbulence intensity in wall flows. *J. Fluid Mech.* **908**.

Cimarelli, A., De Angelis, E., Schlatter, P., Brethouwer, G., Talamelli, A. & Casciola, C. M. 2015 Sources and fluxes of scale energy in the overlap layer of wall turbulence. *J. Fluid Mech.* **771**, 407–423.

DeGraaff, D. B. & Eaton, J. K. 2000 Reynolds-number scaling of the flat-plate turbulent boundary layer. *J. Fluid Mech.* **422**, 319–346.

Hultmark, M. & Smits, A. J. 2021 Scaling turbulence in the near-wall region. *arXiv preprint arXiv:2103.01765* .

Hultmark, M., Vallikivi, M., Bailey, S. C. C. & Smits, A. J. 2013 Logarithmic scaling of turbulence in smooth- and rough-wall pipe flow. *J. Fluid Mech.* **728**, 376–395.

Lee, M. & Moser, R. D. 2015 Direct numerical simulation of turbulent channel flow up to $Re_\tau \approx 5200$. *J. Fluid Mech.* **774**, 395–415.

Lee, M. & Moser, R. D. 2017 Role of large-scale motions in turbulent Poiseuille and Couette flows. In *Proc. 10th Symp. Turb. Shear Flow Phen., Chicago, USA*, *10* 9B-3.

Lee, M. & Moser, R. D. 2018 Extreme-scale motions in turbulent plane Couette flows. *J. Fluid Mech.* **842**, 128–145.

Lee, M. & Moser, R. D. 2019 Spectral analysis of the budget equation in turbulent channel flows at high Reynolds number. *J. Fluid Mech.* **860**, 886–938.

Lozano-Durán, A. & Jiménez, J. 2014 Effect of the computational domain on direct simulations of turbulent channels up to $Re_\tau = 4200$. *Phys. Fluids* **26**, 011702.

Marusic, I., Chandran, D., Rouhi, A., Fu, M., Wine, D., Holloway, B., Chung, D. & Smits, A. J. 2020 A new pathway to turbulent drag reduction. *Under review* .

Marusic, I., Mathis, R. & Hutchins, N. 2010 Predictive model for wall-bounded turbulent flow. *Science* **329**, 193–196.

Mathis, R., Marusic, I., Chernyshenko, S. I. & Hutchins, N. 2013 Estimating wall-shear-stress fluctuations given an outer region input. *J. Fluid Mech.* **715**, 163.

McKeon, B. J., Li, J., Jiang, W., Morrison, J. F. & Smits, A. J. 2004 Further observations on the mean velocity distribution in fully developed pipe flow. *J. Fluid Mech.* **501**, 135–147.

Monkewitz, P. A. 2021 Asymptotics of stream-wise Reynolds stress in wall turbulence. *arXiv preprint arXiv:2104.07322* .

Pirozzoli, S., Bernardini, M. & Orlandi, P. 2014 Turbulence statistics in Couette flow at high Reynolds number. *J. Fluid Mech.* **758**, 327–343.

Pirozzoli, S., Romero, J., Fatica, M., Verzicco, R. & Orlandi, P. 2021 Reynolds number trends in turbulent pipe flow: a DNS perspective. *under review* .

Pope, S. B. 2000 *Turbulent Flows*. CUP.

Samie, M., Marusic, I., Hutchins, N., Fu, M. K., Fan, Y., Hultmark, M. & Smits, A. J. 2018 Fully resolved measurements of turbulent boundary layer flows up to $Re_\tau = 20{,}000$. *J. Fluid Mech.* **851**, 391–415.

Smits, A. J. & Hultmark, M. 2021 Reynolds stress scaling in the near-wall region. *arXiv preprint arXiv:2103.07341* .

Townsend, A. A. 1976 *The Structure of Turbulent Shear Flow*. Cambridge, UK: Cambridge University Press.

Vallikivi, M., Hultmark, M. & Smits, A. J. 2015 Turbulent boundary layer statistics at very high Reynolds number. *J. Fluid Mech.* **779**, 371–389.

Wu, X., Moin, P., Wallace, J. M., Skarda, J., Lozano-Durán, A. & Hickey, J.-P. 2017 Transitional–turbulent spots and turbulent–turbulent spots in boundary layers. *PNAS* **114** (27), E5292–E5299.

Zagarola, M. V. & Smits, A. J. 1998 Mean-flow scaling of turbulent pipe flow. *J. Fluid Mech.* **373**, 33–79.